PAPER

Check for updates

Shape optimization of a meniscus-adherent nanotip†

Shihao Tian, [ID] [a,b] Xudong Chen [ID] [a,b] and Quanzi Yuan [ID] ⋆[a,b]

A soluble tip can dissolve into a tip with curvature when partially immersed in a liquid. This process has been used in the manufacture of sophisticated tips. However, it is difficult to observe the dissolution process in the laboratory, and the dissolution mechanisms at the nanoscale still need to be better understood. Here we utilize molecular dynamics simulations to study the dissolution process of a meniscus-adherent nanotip. The tip apex curvature radius reaches its minimum in the intermediate state. The shape of this state is defined as the optimized shape, which can be used as the termination criterion in applications. In addition, the shape of one optimized tip can be well-fitted to a double-Boltzmann function. The upper Boltzmann curve of this function forms *via* the competition between the chemical potential influence and the intermolecular forces, while the formation of the lower Boltzmann curve is controlled by the chemical potential influence. The parameters of the double-Boltzmann function are strongly correlated with the nanotip's initial configuration and dissolubility. A shape factor ξ is proposed to characterize the sharpness of optimized tips. Theory and simulations show that optimized tips possess a greater ability to shield the capillary effect than common tips. Our findings elucidate the meniscus-adherent nanotip's dissolution process and provide theoretical support for nano-instrument manufacture.

Introduction

When a soluble tip is partially immersed in a liquid, a meniscus forms, and the tip can dissolve into a tip with curvature.[1–3] This process has been widely used in the manufacture of sophisticated tips, such as those used in atomic force microscopy (AFM),[4–7] scanning tunnelling microscopy (STM),[8–10] and nanolithography.[11–13]

However, the tip's formation at the nanoscale is not clearly understood yet. This is attributed to several challenges. First, multiple formation mechanisms can act simultaneously, including the dissolution of the tip, diffusion of the solutes and wetting of the solution on the tip. Second, even though much work has been done on the indirect observation of dissolution,[14,15] the scale of the dissolution process at which the tip shape evolves is atomistic, which hinders direct observation, hiding many details. Besides, theoretical research on tips is based on continuum theory, in which many assumptions are made to simplify calculations.[16–18] Some of these assumptions are not fully applicable to atomic-scale tip-shape

evolution. In the context of these challenges, atomistic modelling serves as a powerful probe to elucidate tip formation mechanisms.

Different applications may have different requirements with respect to the tip profile. The larger aspect ratio of a STM tip contributes to higher reliability of STM images, especially in images of nanometric deep trenches and rough profiles.[19] In the field of dip-pen nanolithography, blunter tips produce higher minimum line widths.[20] Many experimental works have sought to illuminate the influence of etching parameters on the optimized tip shape. Ibe *et al.* employed an electronic cut-off circuit to obtain tips with the radius of curvature varying from approximately 20 to greater than 300 nm.[21] Ju *et al.* obtained a conically shaped tip with a length of up to several millimetres, a controllable tip apex radius, and a specific cone angle *via* static and dynamic etching.[22] Chang *et al.* used a commercial function generator to control the tip length, radius of curvature, surface roughness, and taper angle through modification of etching parameters.[23] Recently, Sun *et al.* proposed a two-step rapid reciprocating etching method to fabricate a tip with a controllable tip length and apex radius to generate a distinct and smooth transition region between the tip and the tip rod.[24] Nevertheless, research on tip mechanical properties such as capillarity and penetrability at the nanoscale is almost non-existent. For AFM operating under ambient conditions,[25–27] well-designed experiments have demonstrated the existence of a meniscus at the relative

ªState Key Laboratory of Nonlinear Mechanics, Institute of Mechanics, Chinese Academy of Sciences, Beijing 100190, China
ᵇSchool of Engineering Science, University of Chinese Academy of Sciences, Beijing 100049, China. E-mail: yuanquanzi@lnm.imech.ac.cn
†Electronic supplementary information (ESI) available. See DOI: https://doi.org/10.1039/d3nr00857f

humidity from 0 to 99%.[28–30] Elegant molecular simulations have also studied the capillary adhesion of nanotips.[31–33] The capillary force of a meniscus can significantly reduce the imaging quality or measurement accuracy;[17,34] Hence, a tip that could reduce the capillary force is preferred.

In this paper, the behaviours of soluble tips with different initial configurations and materials, partially immersed in a liquid, are examined using molecular dynamics (MD) simulations. The evolution of the interface morphology and profile features for different tip widths and dissolubility from the microscopic perspective is discussed. We also quantitatively describe the tip shape features and evaluate the adhesion force of optimized tips. These findings illuminate the mechanisms of meniscus-adherent nanotip dissolution and the characteristics of optimized tips. We believe that this work significantly contributes to dissolution theory and highlights the potential for industrial applications.

Molecular dynamics simulations

Large-scale MD simulations were performed to explore the dissolution of a meniscus-adherent nanotip using LAMMPS code.[35,36] The simulation domain is illustrated in Fig. 1b: a tip with width w is partially immersed in a liquid, and a meniscus emerges because of the capillary force. The initial profile of the meniscus is derived from the profile equation eqn (S4) given in the ESI.† The liquid is modelled as extended simple point charges (SPC/E).[37] The SPC/E model is slightly reparametrized from the simple point charge (SPC) model to add an average polarization correction to the potential energy function, with a modified value of q_O (charge on oxygen atoms) and q_H (charge on hydrogen atoms). The solid is modelled as a face-centred cubic lattice with zero charge. The total potential energy E_{ij} between two coarse particles i and j separated by a distance r_{ij} is composed of short-range van der Waals force energy and long-range coulombic interaction, which are, respectively, calculated by the Lennard–Jones (L–J) potential function and Coulomb's law, as follows:

$$E_{ij} = 4\varepsilon_{ij}\left[\left(\frac{\sigma_{ij}}{r_{ij}}\right)^{12} - \left(\frac{\sigma_{ij}}{r_{ij}}\right)^{6}\right] + k_e\frac{q_iq_j}{r_{ij}} \qquad (1)$$

(where ε_{O-O} = 0.155 kcal mol^{-1}, σ_{O-O} = 0.3166 nm, q_O = −0.8476 e, ε_{H-H} = 0 kcal mol^{-1}, σ_{H-H} = nm, q_H = 0.4238 e, q_S = 0 e, σ_{SS} = 0.264 nm, σ_{SL} = 0.29 nm). ε is the depth of the L–J potential well, σ is the zero-crossing distance for the potential, k_e = 8.988 × 10^9 N m^2 C^{-2} is the Coulomb constant, and q is the charge of one coarse particle. The cut-off length for both the L–J potential and coulombic interaction is 1 nm. The solid–liquid interaction ε_{SL} is fixed to make the solid hydrophilic with the liquid (the equilibrium contact angle is approximately 70°).[38] Simulations for various nanotip widths and dissolubility (w = 59.16, 79.56, 99.96, 120.36, and 140.76 Å, ε = 0.32, 0.4, 0.48, 0.56, 0.64, and 0.72) were conducted;[39] w and ε = $\varepsilon_{SS}/\varepsilon_{SL}$ represent the nanotip width and the ratio of solid–solid and solid–liquid interactions, respectively. The dissolubility of the solid is controlled by ε: a smaller ε generates a higher dissolubility.[40] All the simulations are under periodic conditions. Compared with the fully 3-dimensional system, the 2-dimensional system can produce the expected results with a much smaller number of atoms.

The diffusion coefficient of the solute in the experiment is $D \sim 10^{-9}$ m^2 s^{-1} and the diffusion time is $t_c = a^2/D \sim 10^{-7}$ s,[41] where a is the characteristic length. Therefore, it is impractical to simulate this process (with 10^6 atoms) in MD simulations without acceleration measures that involve huge computing costs.[36] Inspired by the "The FADE mass-stat" proposed by Borg *et al.*, here we regard the simulation system as an open system, and delete atoms on-the-fly within MD simulations.[42] We developed a new strategy for dissolution in MD simulations: the particles with central symmetry parameter (CSP) over 10.37 are regarded as dissolving particles. These particles are deleted during simulation, significantly shortening the simulation time. The detailed criterion for dissolving particles is given in the ESI.† During the whole simulation process, the number of atoms N decreases, while volume V and temperature T remain unchanged. The Nosé–Hoover thermostat[43,44]
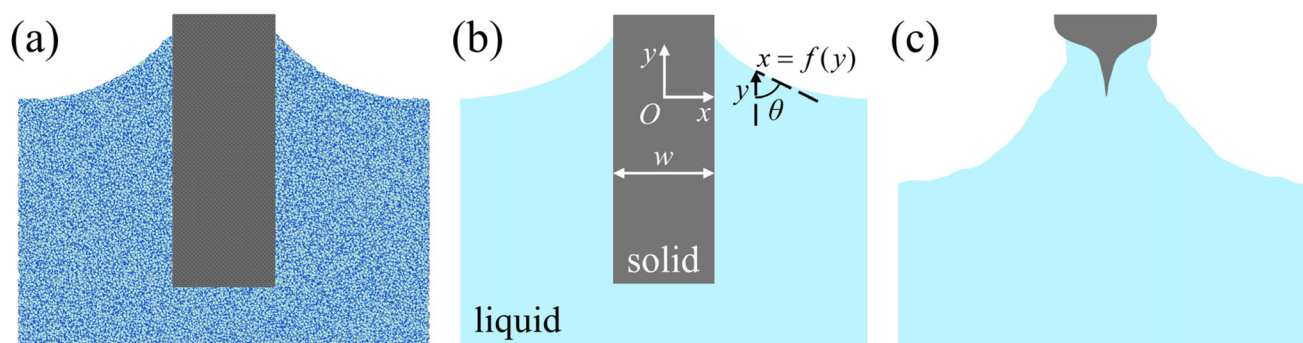
Fig. 1 (a) Atomic view of the simulation domain. Blue balls (hydrogen atoms) and cyan balls (oxygen atoms) depict water molecules. Charcoal grey balls are solid atoms. (b) Surface view of the simulation domain. (c) Surface view of the optimized tip with a meniscus when ε = 0.48 and w = 99.96 Å.

with a time-step of 1 fs was used to regulate the temperature at 450 K,[45] which also accelerates the simulation process.[46]

Results and discussion

Evolution of the solid morphology

During dissolution, solutes can be transported from regions of higher chemical potential to regions of lower chemical potential, which is described by the Cahn–Hilliard equation:[47–49]

$$u_t = \nabla \cdot M(u)\nabla[f(u) - \lambda\Delta u] \quad (2)$$

where $M(u)$ is a mobility coefficient, λ is a coefficient of gradient energy, t is time, and $f(u)$ is a homogeneous free energy. This equation describes phase separation in a two-component system, with u representing the concentration of one of the two components.

The concentration distribution derived from this equation conforms to a Boltzmann distribution. When dissolution starts, all layers in the y-direction have the same amount of dissolving particles, but the gradually varying liquid boundary (different layer thicknesses) generates different local chemical potentials and influences subsequent dissolution, where the layers are different slices (slices' thickness is about 4.08 Å, which is small enough to grasp different features in different layers, and with sufficient atoms to derive properties) of the simulation system in the y-direction, and layer thickness is the thickness of the meniscus of different layers in the x-direction. This explains the evolution of the morphology of the solid. We discuss the dissolution outcomes for $\varepsilon = 0.48$ and $w = 99.96$ Å. A time-sequential contour map of the solid part (tip) during dissolution is shown in Fig. 2a. The area of the solid decreases, and the solid–liquid interface moves toward the solid over time, eventually producing a tip with curvature. The tip can be divided into three parts based on its dissolution features. The upper part has a relatively low dissolution rate because the thin meniscus restricts diffusion, and the dissolution rate

depends on the thickness of the meniscus in different layers in the y-direction. However, the dissolution rate remains almost constant when the thickness of the meniscus is large enough, producing a similar ambient environment. This is the reason for the formation of the middle part. The lower part of the tip is not only in contact with the liquid on the left and right sides of it, but also the liquid under the tip. Therefore, the lower part experiences the most violent dissolution, where the morphology varies from a rectangle to a bullet shape, and then to a sharp apex.

To quantify the changes in the shape of the soluble tip, we investigated the tip apex curvature radius and the tip aspect ratio of different moments (Fig. 2b). The aspect ratio decreases as the dissolution goes on due to the liquid under the tip. Moreover, the curvature radius decreases before 0.83 ns and then increases, indicating that dissolution not only generates a sharp apex but also destroys the apex. Therefore, the sharpest tip is an intermediate state of the shape evolution during dissolution. We define the shape of this state as the optimized shape, and the tip generated at this state as the optimized tip. In application, we care about the sharpness of a tip for the features such as image reliability and resolution.[19,21,50] Therefore, accurately judging the optimized shape is of great significance. It is noteworthy that the tip apex curvature radius cannot be infinitesimal, but that theoretical works[16–18] assume the apex to be infinitely sharp.

Profile of an optimized tip

To elucidate the dissolution mechanisms of a nanotip with a meniscus, here we analyse the optimized shape. For an optimized tip of $\varepsilon = 0.48$ and $w = 99.96$ Å, the symmetrized profile (Fig. 3b) is extracted from Fig. 3a, where we normalize the tip's geometrical shape by dividing the tip's initial width. The profile follows the double-Boltzmann function:

$$x = x_0 + A\left[\frac{p}{1 + e^{\frac{y - y_{01}}{k_1}}} + \frac{1 - p}{1 + e^{\frac{y - y_{02}}{k_2}}}\right] \quad (3)$$
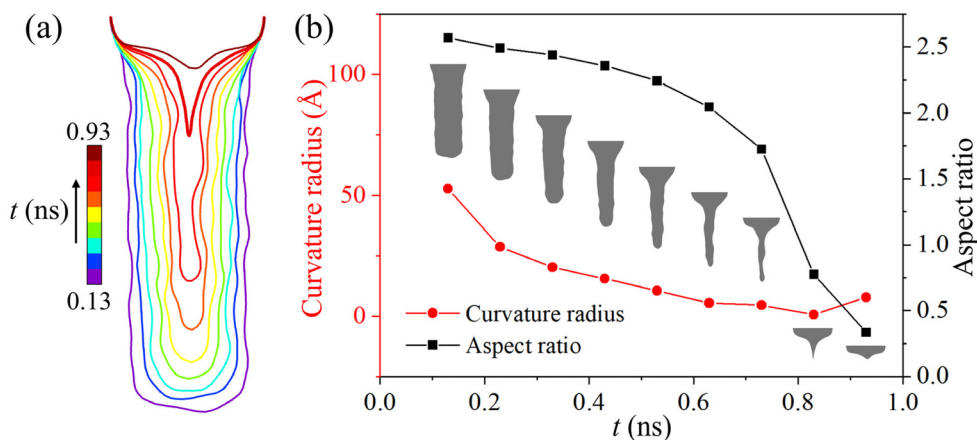
Fig. 2 (a) Time-sequential simulated contour map of the dissolved tip, showing the shape evolution of the nanotip during dissolution (for the sake of observation, here we only show the tip part). (b) Changes in the curvature radius and aspect ratio changes of the nanotip with time. Inset images are the corresponding moments' simulated tip snapshots.
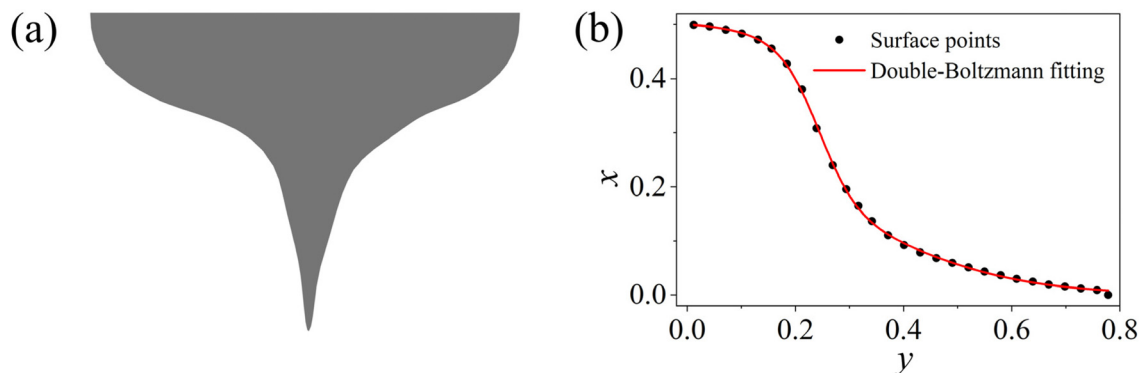
Fig. 3 (a) Snapshot of the optimized tip when ε = 0.48 and w = 99.96 Å. (b) Symmetrized surface points of the optimized tip and its double-Boltzmann fitting. x and y are dimensionless coordinates by dividing the tip's initial width.

where A, x_0, y_{01}, y_{02}, k_1, k_2 and p are the constants obtained by fitting the MD simulated profile data in the present study. A is the span in the y-direction, x_0 is the offset in the x-direction, y_{01} and y_{02} are the centres of both Boltzmann functions, k_1 and k_2 are the slope factors, and p is the fraction of the two Boltzmann functions. When y_{01} and y_{02} are close to each other, the double-Boltzmann curve can be regarded as a non-centrosymmetric Boltzmann curve. Here we call the upward convex part of the double-Boltzmann curve the upper Boltzmann curve and the upward concave part the lower Boltzmann curve.

During dissolution, the width of a nanotip at all layers in the y-direction decreases. Therefore, the capillary force (resultant force of intermolecular forces) decreases, and the meniscus slips slightly to an equilibrium position to balance with gravity (Fig. 1c). This slippage is caused by dissolution and, in turn, influences dissolution. What's more, the thin meniscus at the top of the solid–liquid interface confines the dissolution rate. Therefore, this process is a competition between the chemical potential influence and intermolecular forces. This mechanism is the reason for the formation of the upper Boltzmann curve. In contrast, the lower Boltzmann curve is formed by the chemical potential influence, where the dissolution mechanism is based on the Cahn–Hilliard equation. In the experiment, a tip with initial width = 300 μm is obtained (Fig. 4a–c) from the experiment where a cylindrical tungsten filament vertically immersed into an electrolyte bath dissolves

under external electric fields (details in the ESI†). It is evident that the profile follows a double-Boltzmann function, even though the upper Boltzmann curve is minute compared with the whole tip. If the tip is slender enough, the upper Boltzmann curve makes up a more significant proportion of the whole curve. We used MD simulations to study the nanoscale dissolution process because experiments cannot show the evolution process at such a small scale as the simulations. And this 3 orders-of-magnitude bigger experiment (Fig. 4a–c) was carried out to prove the existence of a double-Boltzmann shape profile and show some size effects between these different length scales.

Size effects of nanotip dissolution

Since the fluctuation phenomenon[51] is more evident at the nanoscale, the contours of a tip at each moment before the optimized shape (0.13–0.73 ns) show much surface fluctuation (Fig. 2a); this is not observable at the macroscale. In addition, these contours all exhibit considerable asymmetry, which is not the case at the macroscale (Fig. 4b). Here we discuss the two parts of the nanotip divided by the apex of the optimized shape. In the lower part, all layers have similar boundary conditions. Hence, the solid–liquid interfaces of the layers advance at almost the same rate. Therefore, dissolution is significantly influenced by the fluctuation phenomenon. This fluctuation phenomenon can promote or inhibit different layers' dissolution. In the upper part of the tip, all layers have
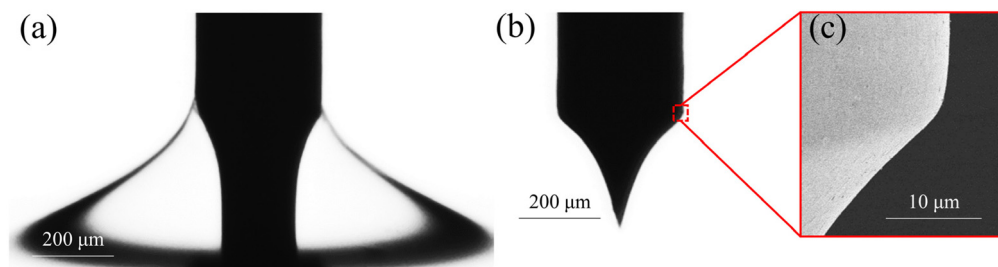
Fig. 4 (a) Experimental snapshot of the tungsten tip's dissolution before slippage of the meniscus. (b) Experimental snapshot of the tungsten tip's dissolution when the meniscus completely slips. (c) Enlarged experimental image of the root of the dissolved tip.

different boundary conditions, so the solid–liquid interface experiences many transformations, weakening the influences of the fluctuation phenomenon. Therefore, dissolution is more active here, creating a smooth solid–liquid interface. In other words, the tip is smooth from the occurrence of the optimized shape. Dissolution is a process in which the surface morphology tends to be ordered.

Unlike the simulation results (Fig. 1c), the movement of the contact line is sometimes too small to be observed in the experiment (Fig. 4a). This is due to the differences in tip size and the contact angle hysteresis[52] caused by surface roughness. The meniscus completely slips down the tip when the tip dissolves to an unstable shape (Fig. 4b). However, this slippage phenomenon is impossible at the scale of the simulations (Fig. 1c). The reason for the difference is that the capillary force is dominant at the nanoscale compared to gravity.

To investigate the influence of tip size on dissolution, we studied nanotips of $\varepsilon = 0.48$ with different widths and performed double-Boltzmann fitting. Optimized tips with different widths are shown in Fig. 5a. Here, we normalize the tip profiles with the same initial width to clearly distinguish the shape differences. As w increases, tip area decreases, and shape becomes "blunter". Moreover, the tip aspect ratio decreases (Fig. 5b). To accurately capture tip properties, the profiles were fitted with a double-Boltzmann function, with constant A, k_1, and k_2. The value of p gradually increases to a stable value as w increases (Fig. 5b). Therefore, parameter p, as a fraction of the two Boltzmann curves, is strongly correlated with the initial size of a tip. This correlation highlights a size effect of dissolution: with increasing width, the normalized profile of a tip for a given ε tends to a stable shape. In other words, if the tips of a given material are large enough, their dissolved shapes under normalization show little difference. Fig. 6f also shows this size effect: the sharpness parameter ξ is almost the same for different ε and when $w > 120$ Å.

The sharpness of optimized tips

Fig. 6a–e show symmetrized contours of optimized tips with different ε and different widths. As ε increases, i.e., the dissolubility of a tip decreases, the dissolution rates in different parts of the tip become similar, and the thin meniscus limit-

ation recedes. For example, the upper Boltzmann curve of an optimized tip with $\varepsilon = 0.72$ and $w = 140.76$ Å (red curve in Fig. 6e) is relatively small, and the transition of the upper and lower Boltzmann curve is almost horizontal; this means that the dissolution rates at different layers in the y-direction are nearly the same. As a result, the sharpness of the whole tip is seemingly the lowest. However, observation of the degree of sharpness is restricted, which may lead to inaccurate results. Therefore, to further study the properties of optimized tips, we combine the size parameter p and slope factors k_1 and k_2 into a new dimensionless parameter, ξ. Here, we define ξ as $\xi = pk_1 + (1 - p)k_2$, which adequately describes the sharpness of an optimized tip. When ξ is relatively large, the transition of the upper and lower Boltzmann curves is smooth. In other words, the tip is integrally sharp. It should be noted that the sharpness discussed here is different from the sharpness used to define the optimized shape, where we only focus on the tip apex curvature radius. Specifically, when ξ is relatively small, the tip is not integrally sharp, but the apex is sharp. It is essential to manage the value of ξ for different purposes in tip manufacturing. ξ for different widths and different ε are shown in Fig. 6f. With increasing ε, ξ decreases, and the tendency is decreasing monotonically. Therefore, we can obtain a tip with a specific sharpness by adjusting the dissolubility of the tip.

The capillary force of the optimized tip and conical tip

The capillary force caused by a meniscus can significantly reduce the imaging quality in AFM, so we investigated the capillary force of an optimized tip and a common conical tip using MD simulations and theory. The capillary force caused by such a liquid meniscus is:[53]

$$F_A = 2\pi\gamma h \tan\varphi \cos(\theta - \varphi) \quad (4)$$

The capillary force can be further written in a dimensionless form:

$$\frac{F_A}{\gamma H} = 2\pi \tan\varphi \cos(\theta - \varphi) \times \frac{h}{H} \quad (5)$$

Here, F_A is the capillary force, γ is the surface tension of the liquid interface, θ is the contact angle, 2φ is the angle
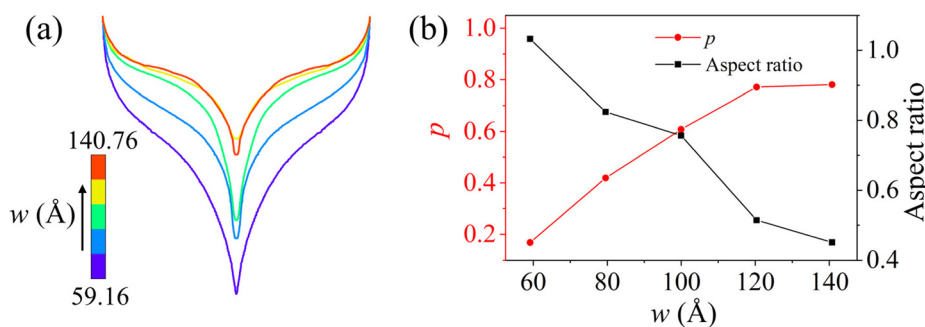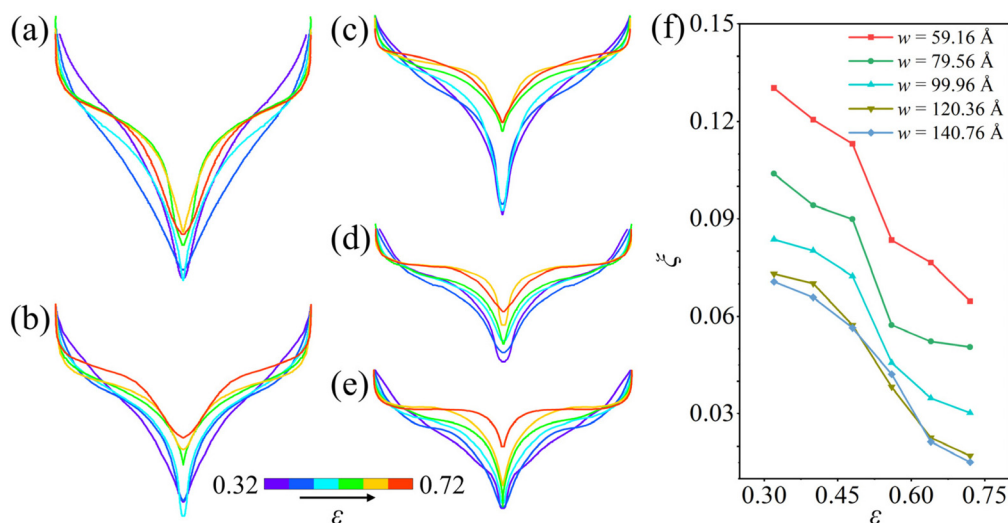

Fig. 5 (a) Symmetrized profiles of optimized tips with different nanotip widths when $\varepsilon = 0.48$. (b) Variations in parameter p and aspect ratio with different w.

Fig. 6 Symmetrized profiles of optimized tips with different ε and widths: (a) w = 59.16 Å, (b) w = 79.56 Å, (c) w = 99.96 Å, (d) w = 120.36 Å, and (e) w = 140.76 Å. (f) ξ changes with different ε and different w.

of the tip, h is the height of the meniscus, and H is the height of the tip. When the tip's contour is not a straight line, φ is not constant and, therefore, controlled by the shape of the contour. According to eqn (5), the capillary force is mainly controlled by the shape factor φ and the material factor θ.

By substituting the shape factors of the optimized tip and the conical tip, the corresponding capillary forces are obtained (Fig. 8b). The capillary force on the optimized tip is much smaller than that on the conical tip with increasing depth. Meanwhile, we used MD simulations to calculate the capillary force of the optimized tip and of the conical tip. We put an optimized tip and a common conical tip plugging into the liquid with m varying among 0, 0.13, 0.27, 0.4, 0.53, and 0.67, where m represents the ratio of the tip's initial plugging depth and width. When the energy of the simulated system reaches the stable state, we record the snapshots of the simulated regions (Fig. 7b and c) and calculate the normalized capillary force F^* (Fig. 8a), where F^* is the ratio of the capillary force calculated by MD simulations and its maximum with different m. The capillary force of the two tips increases

with time, but the optimized tip carries a smaller capillary force, which is consistent with the theoretical results in Fig. 8b. Due to the roughness of atomic surface, the surface of the optimized tip is coarser than that of a conical tip. When the liquid climbs along the optimized tip, the vibrating liquid particles tend to stick to the solid particles and do not slip down due to the surface roughness. Therefore, the liquid on the optimized tip climbs higher than the liquid on the tip whose surface has the same profile with the optimized tip but is ideally smooth. Surface roughness is also the reason why the simulated capillary force of the optimized tip increases faster than that in the theoretical results when h/H increases.

In applications such as AFM, the measurement accuracy can be greatly affected by the capillary force, which is influenced by the ambient conditions on the sample surface (m = 0). In Fig. 7b and c, the climbing area of the meniscus of the optimized tip is much smaller than that of the conical tip when the plugging depth is 0. Moreover, the results from MD simulations show that using an optimized tip reduces the capillary force of a liquid film environment (m = 0) by 82%
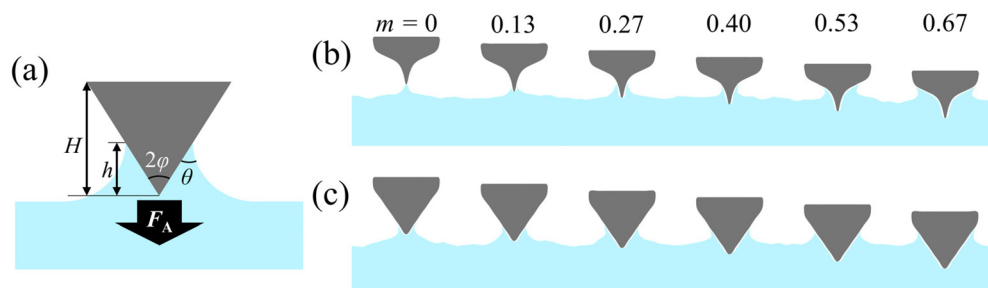
Fig. 7 (a) Schematic diagram of a meniscus adhering to a nanotip. (b) Simulated snapshots of stable states of an optimized tip with different initial plugging depths. (c) Simulated snapshots of stable states of a conical tip with different initial plugging depths.
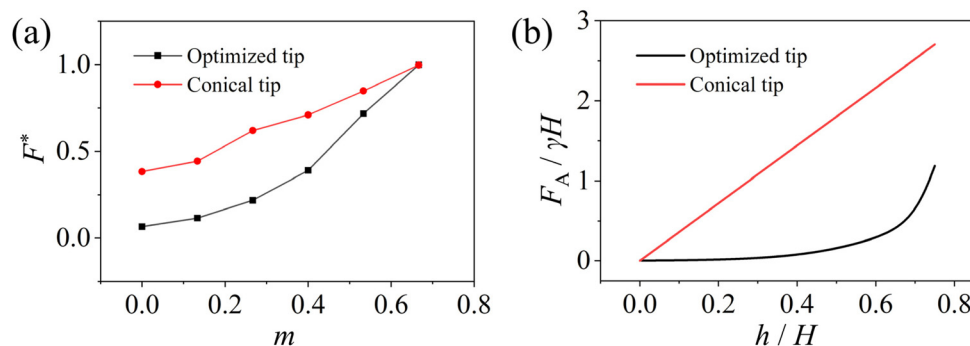
Fig. 8 (a) Capillary forces with different initial plugging depths calculated by MD simulations. (b) Capillary forces with different climbing heights calculated using eqn (5).

when using a conical tip as a benchmark. Furthermore, an optimized tip can be cut and glued to an AFM probe, preventing adhesion of the liquid.[17] Therefore, the special shape of an optimized tip reduces the capillary effect.

Conclusions

The dissolution of a meniscus-adherent nanotip was studied using molecular dynamics simulations. The results show that the apex curvature radius decreases and then increases, reaching a minimum in the intermediate state. We defined the shape of this state as the optimized shape, which could be used as the termination criterion in applications. The tip shape is well-fitted with a double-Boltzmann function. The upper Boltzmann curve arises *via* the competition between the chemical potential influence and intermolecular forces, while the lower Boltzmann curve is controlled by the chemical potential influence. The parameters of the double-Boltzmann function have a strong correlation with the initial configuration and dissolubility of the nanotip. A shape factor ξ is proposed to measure the sharpness of a dissolved tip. An optimized tip generates a smaller adhesion force than a common tip. Our findings elucidate meniscus-adherent nanotip dissolution and provide a theoretical guide for the fabrication of nano-instruments.

Author contributions

Q. Y. designed the research; S. T. performed the MD simulations; X. C. performed the experiments; and S. T. and Q. Y. analysed the data and wrote the manuscript. All the authors discussed the results and commented on the manuscript.

Conflicts of interest

There are no conflicts to declare.

Acknowledgements

References

1 P. J. Bryant, H. S. Kim, Y. C. Zheng and R. Yang, *Rev. Sci. Instrum.*, 1987, **58**, 1115–1115.
2 D. Xu, K. M. Liechti and K. Ravi-Chandar, *Rev. Sci. Instrum.*, 2007, **78**, 073707.
3 M. Kulakov, I. Luzinov and K. G. Kornev, *Langmuir*, 2009, **25**, 4462–4468.
4 G. Binnig, C. F. Quate and C. Gerber, *Phys. Rev. Lett.*, 1986, **56**, 930–933.
5 C. Gerber and H. P. Lang, *Nat. Nanotechnol.*, 2006, **1**, 3–5.
6 D. Alsteens, H. E. Gaub, R. Newton, M. Pfreundschuh, C. Gerber and D. J. Müller, *Nat. Rev. Mater.*, 2017, **2**, 17008.
7 M. Krieg, G. Fläschner, D. Alsteens, B. M. Gaub, W. H. Roos, G. J. L. Wuite, H. E. Gaub, C. Gerber, Y. F. Dufrêne and D. J. Müller, *Nat. Rev. Phys.*, 2019, **1**, 41–57.
8 G. Binnig and H. Rohrer, *Rev. Mod. Phys.*, 1987, **59**, 615–625.
9 S.-i. Kitamura, T. Sato and M. Iwatsuki, *Nature*, 1991, **351**, 215–217.
10 B. Jäck, Y. Xie and A. Yazdani, *Nat. Rev. Phys.*, 2021, **3**, 541–554.
11 Y. F. Lu, Z. H. Mai, G. Qiu and W. K. Chim, *Appl. Phys. Lett.*, 1999, **75**, 2359–2361.
12 R. D. Piner, J. Zhu, F. Xu, S. Hong and C. A. Mirkin, *Science*, 1999, **283**, 661–663.
13 E. Albisetti, A. Calò, A. Zanut, X. Zheng, G. M. de Peppo and E. Riedo, *Nat. Rev. Methods Primers*, 2022, **2**, 32.
14 C. Ritschel, J. Napp, F. Alves and C. Feldmann, *Nanoscale*, 2022, **14**, 16249–16255.

15 J. H. Yang, Q. Z. Yuan and Y. P. Zhao, *Sci. China: Phys., Mech. Astron.*, 2019, **62**, 124611.

16 Y. Ge, W. Zhang, Y.-L. Chen, C. Jin and B.-F. Ju, *J. Mater. Process. Technol.*, 2013, **213**, 11–19.

17 J. H. Yang and Q. Z. Yuan, *Adv. Mater. Interfaces*, 2022, **9**, 2201248.

18 X. D. Chen and Q. Z. Yuan, *Adv. Mater. Interfaces*, 2023, **10**, 2202380.

19 G. Tahmasebipour, Y. Hojjat, V. Ahmadi and A. Abdullah, *Int. J. Adv. Manuf. Technol.*, 2009, **44**, 80–90.

20 J. Haaheim, R. Eby, M. Nelson, J. Fragala, B. Rosner, H. Zhang and G. Athas, *Ultramicroscopy*, 2005, **103**, 117–132.

21 J. P. Ibe, P. P. Bey, S. L. Brandow, R. A. Brizzolara, N. A. Burnham, D. P. Dilella, K. P. Lee, C. R. K. Marrian and R. J. Colton, *J. Vac. Sci. Technol., A*, 1990, **8**, 3570–3575.

22 B. F. Ju, Y. L. Chen and Y. Z. Ge, *Rev. Sci. Instrum.*, 2011, **82**, 013707.

23 W.-T. Chang, I.-S. Hwang, M.-T. Chang, C.-Y. Lin, W.-H. Hsu and J.-L. Hou, *Rev. Sci. Instrum.*, 2012, **83**, 083704.

24 Y. M. Sun, H. W. Deng, X. Y. Liu and X. M. Kang, *Rev. Sci. Instrum.*, 2022, **93**, 123304.

25 Y. F. Dufrene and A. E. Pelling, *Nanoscale*, 2013, **5**, 4094–4104.

26 D. M. Arvelo, M. R. Uhlig, J. Comer and R. Garcia, *Nanoscale*, 2022, **14**, 14178–14184.

27 R. An, A. Laaksonen, M. Q. Wu, Y. D. Zhu, F. U. Shah, X. H. Lu and X. Y. Ji, *Nanoscale*, 2022, **14**, 11098–11128.

28 L. Sirghi, R. Szoszkiewicz and E. Riedo, *Langmuir*, 2006, **22**, 1093–1098.

29 B. L. Weeks, M. W. Vaughn and J. J. DeYoreo, *Langmuir*, 2005, **21**, 8096–8098.

30 S. Rozhok, P. Sun, R. Piner, M. Lieberman and C. A. Mirkin, *J. Phys. Chem. B*, 2004, **108**, 7814–7819.

31 J. Jang, G. C. Schatz and M. A. Ratner, *Phys. Rev. Lett.*, 2004, **92**, 085504.

32 H. Kim, B. Smit and J. Jang, *J. Phys. Chem. C*, 2012, **116**, 21923–21931.

33 M. Watkins and B. Reischl, *J. Chem. Phys.*, 2013, **138**, 154703.

34 X. H. Chen, B. W. Li, Z. X. Liao, J. D. Li, X. M. Li, J. Yin and W. L. Guo, *Adv. Mater. Interfaces*, 2022, **9**, 2201864.

35 S. Plimpton, *J. Comput. Phys.*, 1995, **117**, 1–19.

36 A. P. Thompson, H. M. Aktulga, R. Berger, D. S. Bolintineanu, W. M. Brown, P. S. Crozier, P. J. in 't Veld, A. Kohlmeyer, S. G. Moore, T. D. Nguyen, R. Shan, M. J. Stevens, J. Tranchida, C. Trott and S. J. Plimpton, *Comput. Phys. Commun.*, 2022, **271**, 108171.

37 H. Berendsen, J. R. Grigera and T. Straatsma, *J. Phys. Chem.*, 1987, **91**, 6269–6271.

38 Q. Z. Yuan, J. H. Yang, Y. Sui and Y. P. Zhao, *Langmuir*, 2017, **33**, 6464–6470.

39 Q. Miao and Q. Z. Yuan, *Phys. Chem. Chem. Phys.*, 2023, **25**, 7487–7495.

40 Q. Miao, Q. Z. Yuan and Y. P. Zhao, *Phys. Fluids*, 2020, **32**, 102103.

41 A. D. Davydov, A. P. Grigin, V. S. Shaldaev and A. N. Malofeeva, *J. Electrochem. Soc.*, 2002, **149**, E6–E11.

42 M. K. Borg, D. A. Lockerby and J. M. Reese, *J. Chem. Phys.*, 2014, **140**, 074110.

43 S. Nosé, *Mol. Phys.*, 1984, **52**, 255–268.

44 W. G. Hoover, *Phys. Rev. A*, 1985, **31**, 1695–1697.

45 S. H. Lee, *Bull. Korean Chem. Soc.*, 2013, **34**, 3800–3804.

46 M. Peleg, M. D. Normand and M. G. Corradini, *Crit. Rev. Food Sci. Nutr.*, 2012, **52**, 830–851.

47 J. W. Cahn and J. E. Hilliard, *J. Chem. Phys.*, 1958, **28**, 258–250.

48 J. W. Cahn, *Acta Metall.*, 1961, **9**, 795–801.

49 A. Novick-Cohen, *Handbook of Differential Equations. IV Evolutionary Partial Differential Equations*, 2008.

50 A. Boisen, O. Hansen and S. Bouwstra, *J. Micromech. Microeng.*, 1996, **6**, 58–62.

51 E. M. Sevick, R. Prabhakar, S. R. Williams and D. J. Searles, *Annu. Rev. Phys. Chem.*, 2008, **59**, 603–633.

52 D. Quéré, *Annu. Rev. Mater. Res.*, 2008, **38**, 71–99.

53 D. S. Guan, E. Charlaix and P. E. Tong, *Phys. Rev. Lett.*, 2020, **124**, 188003.